Exp Fluids
DOI 10.1007/s00348-009-0745-z

RESEARCH ARTICLE

Volumetric velocity measurements of vortex rings from inclined exits

Daniel R. Troolin · Ellen K. Longmire

Received: 16 October 2008 / Revised: 9 September 2009 / Accepted: 10 September 2009

Abstract Vortex rings were generated by driving pistons within circular cylinders of inner diameter $D = 72.8$ mm at a constant velocity U_0 over a distance $L = D$. The Reynolds number, $U_0L/(2\nu)$, was 2500. The flow downstream of circular and inclined exits was examined using volumetric 3-component velocimetry (V3V). The circular exit yields a standard primary vortex ring that propagates downstream at a constant velocity and a lingering trailing ring of opposite sign associated with the stopping of the piston. By contrast, the inclined nozzle yields a much more complicated structure. The data suggest that a tilted primary vortex ring interacts with two trailing rings; one associated with the stopping of the piston, and the other associated with the asymmetry of the cylinder exit. The two trailing ring structures, which initially have circulation of opposite sign, intertwine and are distorted and drawn through the center of the primary ring. This behavior was observed for two inclination angles. Increased inclination was associated with stronger interactions between the primary and trailing vortices as well as earlier breakdown.

Electronic supplementary material The online version of this article (doi:10.1007/s00348-009-0745-z) contains supplementary material, which is available to authorized users.

D. R. Troolin (✉)
Fluid Mechanics Division,
TSI Incorporated, St. Paul, MN, USA
e-mail: dan.troolin@tsi.com

E. K. Longmire
Department of Aerospace Engineering & Mechanics,
University of Minnesota, Minneapolis, MN, USA
e-mail: ellen@aem.umn.edu

1 Introduction

Vortex rings generated by impulses occur in many environmental, biological, and industrial applications. The flow associated with vortex rings generated from axisymmetric boundary conditions has been studied extensively (see Didden 1979; Gharib et al. 1998; and the reviews by Shariff and Leonard 1992; Lim and Nickels 1995, for example). In many applications, however, the boundary conditions are not axisymmetric, and therefore the effects of asymmetry on the resulting vortex development, propagation, and breakdown are of interest. In the current study, we examine the effect of inclined trailing edge geometry on vortex ring development.

Vortex rings initiated downstream of cylinders with inclined exits were first examined by Webster and Longmire (1998) using planar particle image velocimetry (PIV). The authors viewed instantaneous slices of flow in different azimuthal planes to reconstruct a picture of the overall flow behavior. The reconstruction consisted of a complex vortex structure including a primary ring and additional tubes of vorticity that initially extended upstream into the cylinder and subsequently passed through the primary ring. The additional tubes were thought to be initiated at the short side of the cylinder where entrainment into the primary ring was strongest. The strength of the additional tubes increased with increasing trailing edge angle. Also, the overall propagation speed and penetration distance of the primary vortex decreased with increasing trailing edge angle. In a flow visualization study on rings initiated from similar cylinders, Lim (1998) noted the presence of circumferential flow within the primary ring cores, and proposed several processes by which core breakdown occurs. In the present work, we employ a volumetric 3-component velocimetry (V3V) system to

Published online: 22 September 2009

examine the evolving three-dimensional flow structure directly. As will be shown below, this technique confirms some of the behavior postulated by Webster and Longmire, but also reveals new dynamics of the flow that were not known or understood previously.

2 Experimental facility and methods

2.1 Facility

The experiments were conducted in a water-filled glass tank of square cross section with 600 mm sides and 600 mm depth. Vortex rings were generated by displacing a piston through submerged cylinders with flat and inclined exits. The inner diameter (D) of the cylinders was 72.8 mm with wall thickness of 1.7 mm. The inclined exits were cut so that the axial distances between the longest and shortest lip locations were $D/4$ (14°) and $D/2$ (26°). The piston, which was axisymmetric, was actuated to travel at nearly constant velocity of 66.2 mm/s for a distance $L = D$ before stopping abruptly at a final location D upstream of the average cylinder lip location. The vortex generating apparatus is described in detail in Webster and Longmire (1998). The plots shown are normalized by the cylinder diameter, and the time increment is consistent with that used by Webster and Longmire, where $t^* = (t - t_0)U_0/L$, t_0 is the time when the piston begins moving, L is the stroke length, and U_0 is the constant piston velocity. Also, in keeping with the conventions of Webster and Longmire, the angle ψ is defined to be zero at the location where the cylinder lip was longest, and $\psi = \pi$ where it was shortest, and the flow Reynolds number is defined as Γ_0/ν where $\Gamma_0 = U_0 L/2$. In the current experiments, the Reynolds number was held fixed at 2500, which is slightly lower than the value of 2800 associated with Webster and Longmire's PIV measurements.

2.2 Experimental methods

The volumetric 3-component velocimetry (V3V) technique described by Pereira et al. (2000) was used to determine velocity fields within volumes downstream of the cylinder exit. A schematic representation of the experimental setup can be seen in Fig. 1. The flow was illuminated by a dual-head Nd:YAG laser with 200 mJ/pulse. Two negative 25-mm cylindrical lenses were mounted in front of the beam exit in perpendicular orientations to produce an ellipsoidal cone of laser light. A flat mirror reflected the light by 90° into the water tank, and a second mirror on the opposite side of the tank was used to reflect light back toward the measurement region to increase the illumination intensity. Beam blocks were used to limit the horizontal thickness of the illumination volume to approximately 120 mm. Polycrystalline particles with a mean diameter of approximately 50 μm were used as the tracers.

The volumetric camera (shown in blue in Fig. 1) consisted of three apertures arranged in an equilateral triangle of side length 170 mm, each containing a CCD array with four million pixels (2,048 × 2,048) of size 7.4 microns and depth 12 bits. Three 50-mm Nikon camera lenses were used with aperture settings of f#16. The camera was mounted at an optical distance of 701 mm from the back plane of the measurement region at 90° to the illuminating light. The camera field of view allowed for a measurement region of 140 mm in the horizontal and vertical directions.

The V3V camera frames and laser pulses were triggered by a TSI 610035 synchronizer with 1 ns time resolution. Each of the three apertures captured pairs of images. The two lasers emitted pulses timed to straddle neighboring camera frames in order to produce images suitable for 3D particle tracking. The time between frame-straddled laser pulses (Δt) was 3,500 μs. The synchronizer was triggered externally to coincide with the initiation of the piston stroke. Image sets were then captured at a rate of 7.25 Hz, so that the time increment between fields was $t^* = 0.125$.

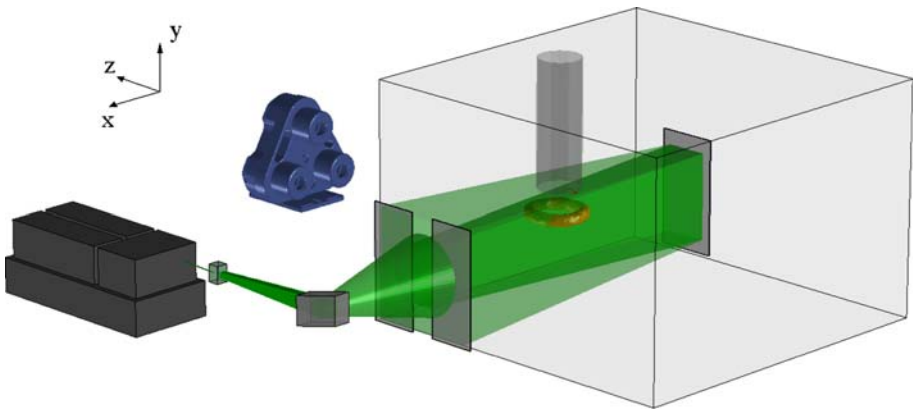

Fig. 1 Schematic of experimental setup

The images were streamed directly to a set of six hard drives, bypassing the computer bus and allowing capture at the full frame rate of each CCD device.

Instantaneous velocity fields were determined in four steps: identification of 2D particle locations from each of three apertures, determination of 3D particle locations in space, tracking of individual particles in the volume, and interpolation of the resulting randomly spaced vectors onto a Cartesian grid. The details of each step are given in the following section.

2.2.1 2D particle identification

A single V3V capture includes three image pairs. The locations of tracer particles in each image were determined by setting a baseline intensity threshold of 50 (out of 4,096 gray scales), a minimum and maximum 2D particle diameter of 2 and 4 pixels, respectively, and a maximum particle overlap value of 50%. A Gaussian intensity profile was fitted to each particle image, and the peak represented the center of the particle. An example of one of the V3V images from the top camera aperture can be seen in Fig. 2, which clearly shows the seeding density. Note that the particle density in the image appears very similar to that in PIV (particle image velocimetry) images, although PIV images typically cover only a thin volume depth of order 1 mm, while the current V3V image covers a depth of 120 mm. Therefore, the volumetric seeding density for V3V is lower than that of PIV. The seeding density of standard 2D planar PIV is ideally greater than ten particles per interrogation region (Keane and Adrian 1990). Assuming an interrogation size of 4 mm^2 and a light sheet thickness of 1 mm, this would correspond to a seeding density of 625 particles/cm^3. In the current study, the seeding density was approximately 60 particles/cm^3, or 1/10th that of PIV.

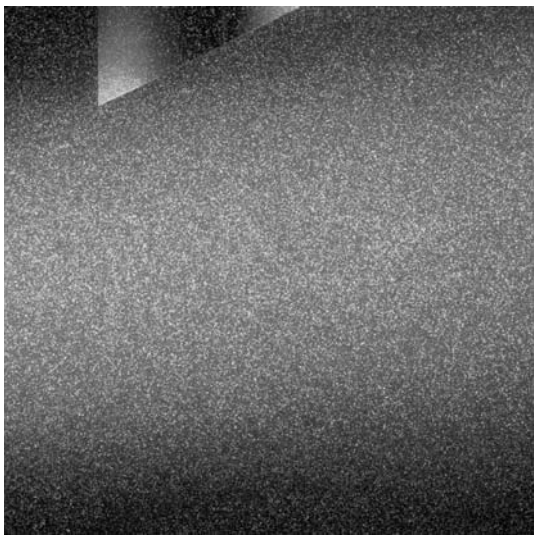

Fig. 2 Particle image from top aperture downstream of $D/2$ cylinder

2.2.2 3D particle identification

The correspondence of a 2D particle in one image to the same particle in the other two images was achieved by referencing particle images to a volumetric spatial calibration. The spatial calibration was determined by traversing a single-plane target through the measurement region and capturing images at regular intervals. Dots on the calibration target were spaced regularly at 5 mm in the horizontal (x) and vertical (y) directions, and the target was traversed by 2.5 mm increments in the depth (z) direction. The plane at which the axes of all three camera apertures intersect is called the reference plane. In a perfect camera, a calibration dot lying on the reference plane would lie at the same x and y pixel location in each image. As the calibration target is moved toward the camera, the calibration dot image location on each sensor begins to diverge outward in the form of a triangle. The calibration dot locations from each image were combined to define a camera signature graph, in which a unique triangle size was determined for each plane.

Consider Fig. 3 in which a schematic representation of the 3D particle identification step is shown. For clarity, images from the left (L), right (R), and top (T) apertures are shown overlapped. Particle images from the left image are white, particle images from the right image are red, and particle images from the top image are blue. Consider a 2D particle as seen by the left aperture. A single dot in the left aperture corresponds with a ray in the top and right apertures. The 3D location algorithm searches along these defining rays (shown as dashed arrows) in the top and right images simultaneously for possible 2D particle matches. A valid triplet is one in which the 2D particles from all three images fall within a tolerance of 0.5 pixels of the triangle defined by the signature graph. The centroid of the triplet then represents the x and y location, and the size of the triangle gives the z location. This process is repeated for all particles in the field.

2.2.3 3D particle tracking

The 3D particle tracking algorithm is a relaxation method based upon the work of Ohmi and Li (2000) and Pereira et al. (2006). Once the volumetric particle locations are determined in frame A and frame B, the particles are divided into subgroups called "clusters" according to their spatial locations. Clusters here can be thought of as similar to interrogation regions in PIV and typically contain approximately eight particles. Clusters in B are larger in volume than corresponding clusters in A because particles may move out of the initial cluster volume. Within a

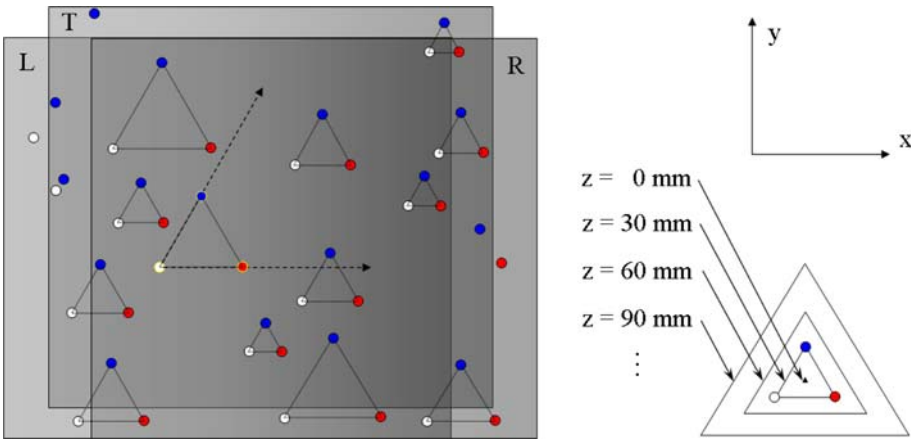

Fig. 3 Schematic representation of 3D particle identification. Particle images from the *left* image (L) are represented by *white*, particle images from the *right* image (R) by *red*, and particle images from the *top* image (T) by *blue*. The centroid of the triplet represents the x and y location, and the size gives the z location

cluster, each pair of corresponding particles is assigned a number representing match probabilities. For example, P(m,n) is the match probability between particle m in frame A and particle n in frame B. Initially, each particle pair has the same probability, $1/N$, where N is the number of possible pairs between A and B for each cluster. The probability computation is based on the assumption that neighboring particles move similarly. These probabilities are then iteratively recomputed for all particles in the cluster, until they converge. As a result of this iteration, the correct matching probability is increased almost to unity while the others tend to zero. For particle m in frame A, the maximum match probability P(m,n) is found among P(m,1), P(m,2),…. Then (m,n) is a matched pair.

2.2.4 Grid interpolation

The vectors determined by the 3D particle tracking step were spaced randomly according to particle locations. In order to compute quantities such as vorticity and swirl, it was useful to have vectors on a Cartesian grid. Vorticity was calculated using central-differencing on the rectangular grid of velocities. These vectors were found through regular Gaussian-weighted interpolation, where the Gaussian radius extended to the voxel corners. In the experiments described, the resulting measurement volume was approximately 140 × 140 × 120 mm. A typical single capture yielded between 30,000 and 40,000 independent randomly spaced velocity vectors, for an average spatial resolution of approximately 4 mm. The vectors were then interpolated onto a rectangular grid with 4 mm vector spacing, which resulted in nearly 37,000 vectors per instantaneous velocity field.

3 Results

In the following plots, isosurfaces of vorticity magnitude (ω) are used to visualize vortical structures. In addition to vorticity magnitude, slices of 2D vorticity and slices of signed 3D (λ_{3D}) and 2D swirl strength (λ_{2D}), defined as the imaginary part of the eigenvalue of the three-dimensional and in-plane velocity gradient tensor, respectively (Zhou et al. 1999), were examined. The swirl strength is a positive scalar that identifies regions swirling about an axis (as opposed to shearing regions). In the planar plots shown below, λ_{2D} has been given a sign based on the sign of the local 2D vorticity.

3.1 Flat cylinder

Velocity data generated from the standard cylinder with flat exit reveal a primary ring that is initially axisymmetric with diameter of 1.25 D. The ring propagates downstream at constant speed, corresponding closely with the previous PIV results of Webster and Longmire (1998) at similar Reynolds number. Vorticity magnitude isosurfaces for this case at a relatively early time, $t^* = 2.13$, are shown in Fig. 4, and the vortex propagation is shown in Supplementary Movie 1 from $t^* = 0$ to 7.52. Note that all data plots are presented in cartesian coordinates with $-y$ aligned in the streamwise direction. The plot on the left shows an off-axis perspective view of the flow with the cylinder depicted in gray. The plot on the right is a view from beneath the primary ring, looking up toward the cylinder exit. The larger primary ring results from the sudden impulse of the piston, which forces a slug of fluid through and out of the cylinder. Boundary layers form on the inside and outside walls of the cylinder (see e.g. Didden 1979), and as the slug of fluid separates from the nozzle lip, a cylindrical sheet of vorticity rolls up into a coherent ring. At $t^* = 2.13$, the primary ring is located approximately 0.4 D downstream of the cylinder exit. The rotation of this ring is such that fluid is drawn downward through its center. Upstream of the primary ring, a weaker stopping vortex ring is observed near the exit lip. The stopping ring, which has rotation opposite that of the primary ring, results from the termination of the piston motion. When the piston

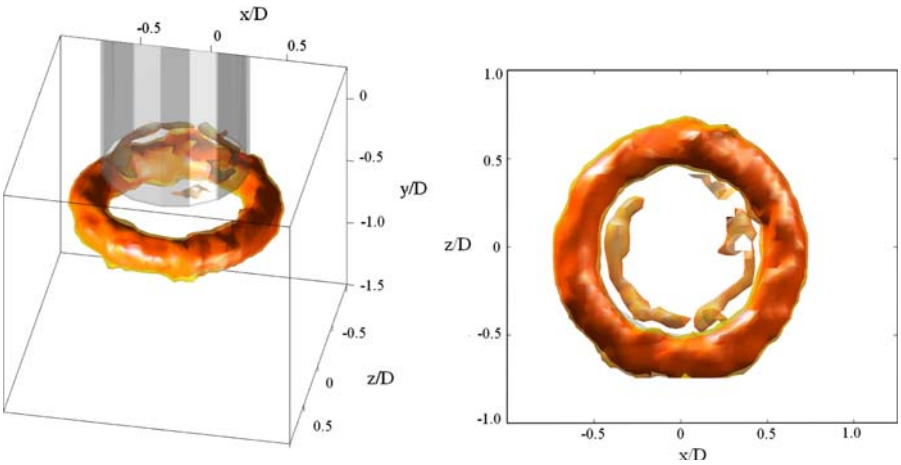

Fig. 4 Vorticity magnitude isosurfaces for the standard cylinder at $t^* = 2.13$. Isosurfaces are at values of $\omega D/U_0 = 4.4$ (*orange*) and 6.1 (*red*)

stops, by continuity, the fluid within the cylinder stops also, and surrounding fluid is entrained inward at the cylinder lip generating the opposing ring. The self-induction associated with this ring is in the upstream direction, and it stalls and dissipates near the nozzle exit. A similar stopping vortex ring is visualized in detail and described by Didden (1979).

In addition to the primary and stopping vortex rings, a piston vortex ring must also be generated. The piston vortex ring, which has the same rotation direction as the primary ring, forms along the inner wall of the cylinder downstream of the advancing piston. The piston vortex has been well documented in the literature for axisymmetric cylinder exit geometries; see for example Allen and Chong (2000), Allen and Auvity (2002), and Cater et al. (2004). Allen and Auvity found that when the piston end stops further than 0.3 D upstream of the cylinder exit, the piston vortex remains confined within the cylinder, and a stopping vortex forms at the cylinder exit with circulation opposite that of the primary and piston vortices. The authors also found that when the piston end stops flush with the cylinder exit, the stopping vortex is eliminated, and the piston vortex is ejected and entrained into the primary ring where it is rapidly strained and convected around the periphery of the primary vortex core, increasing the overall circulation. In the current study, the piston motion ceases a distance, D, upstream of the cylinder exit; therefore, the piston vortex remains within the cylinder and is not observed in Fig. 4 (or Supplementary Movie 1).

Vortex rings generated from axisymmetric boundary conditions have been studied extensively in the literature (e.g. Shariff and Leonard 1992; Lim and Nickels 1995; Gharib et al. 1998; Krueger 2005). The evolution of the primary ring is fairly well understood, though typically, little focus has been placed on the characteristics of the stopping ring. Didden (1979) and others have shown that for laminar vortex rings generated by moving pistons, the primary ring typically propagates downstream stably with a speed that decays slowly due to viscous diffusion, and its motion is decoupled from the stopping ring, which remains in the vicinity of the origin. By contrast, Dabiri et al. (2005) showed that starting and trailing vortices generated by swimming (deforming) jellyfish are coupled.

3.2 $D/2$ cylinder

Although the flow downstream of the $D/2$ cylinder shares some of the basic features of the axisymmetric case, including a primary ring and trailing vortical structures, the overall organization is highly complex and three-dimensional. For this reason, even the dominant structures are difficult to depict and track using a single quantity. Therefore, volumetric plots and movies of vorticity magnitude, slices of vorticity, and slices of signed two-dimensional swirl have all been implemented to aid in the discussion. Also, the following description is based on analysis of volumetric movies and plots viewed from additional angles, not included below.

Vortex ring formation downstream of the $D/2$ cylinder begins in somewhat the same way as for the axisymmetric case. A primary ring begins developing downstream of the cylinder edge while the piston is in motion ($t^* < 1$). The ring circulation is greater at the upstream lip ($\psi = \pi$) than at the downstream lip ($\psi = 0$) due to asymmetries in the velocity exiting the cylinder as well as asymmetries in entrainment (see Webster and Longmire 1998). For example, at $\psi = \pi$, the primary ring has separated from the lip by $t^* = 0.7$ while at $\psi = 0$, the ring remains attached (Webster and Longmire 1998; Fig. 5b).

The primary ring detachment on the $\psi = \pi$ side of the cylinder is accompanied by entrainment of fluid drawn in toward the cylinder axis on this side. This sweep of incoming fluid is strongest along the plane of symmetry and weaker as the distance from the symmetric plane increases. This velocity gradient causes counter-rotating

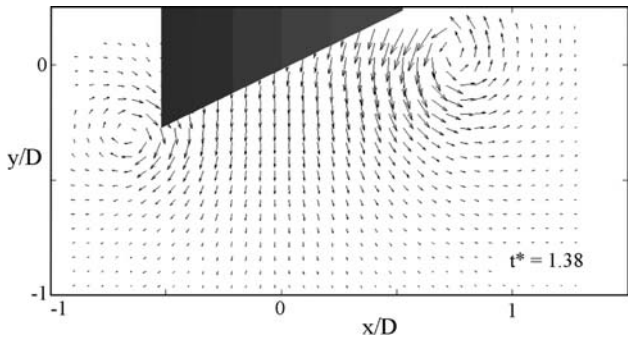

Fig. 5 Vector slice along the symmetric plane of the $D/2$ cylinder at $t^* = 1.38$

vorticity, which results in swirling tubes that extend from the primary ring on either side of $\psi = \pi$, up into the cylinder exit. The existence of these tubes of vorticity helps explain why the circulation around the primary core at $\psi = \pi$ is larger than the circulation around what appears to be the same core at $\psi = \pi/2$ and $3\pi/2$ (see Webster and Longmire).

After the piston stops at $t^* = 1$, the primary ring separates entirely from the cylinder lip, and, as with the flat cylinder case described previously, fluid is entrained inward around and immediately downstream of the lip, as can be seen in Fig. 5, which shows a vector slice at $t^* = 1.38$. This phenomenon is also observable in the plots of Webster and Longmire at similar t^* values. This inward entrainment of fluid between the fluid remaining in the cylinder and the fluid propagating downstream must create a stopping vortex ring on the inner part of the cylinder at the lip (see visualization in Didden 1979). The piston ring must continue to propagate downward, away from the piston face but likely remains inside of the cylinder. In the case of the flat cylinder exit, the distance from the stopped piston to the cylinder exit is D. In the $D/2$ case, the distance from the stopped piston to the $\psi = \pi$ lip location is shorter (0.75 D) but still significantly longer than the minimum 0.3 D found by Allen and Auvity (2002) as required for expulsion of a piston vortex.

A time progression of the flow structure resulting from the $D/2$ cylinder can be seen in Fig. 6 and in Supplementary Movies 2a and 2b from $t^* = 0$ to 7.52. Volumetric data in Fig. 6 are depicted starting at $t^* = 2.13$, since prior to this point, most of the vortex interactions remain inside the cylinder, out of the measurement field of view. In the figure, time progresses from top to bottom and adjacent plots show different views of the same time. A schematic drawing of our interpretation of coherent structures present at each time is shown in the left column (i); the primary vortex ring is yellow, the stopping vortex ring is aqua, and a third vortical structure associated with the tubes generated by the asymmetry in the cylinder exit is green. The center column (ii) contains volumetric plots of vorticity magnitude looking downward and from the side. The right column (iii) contains volumetric plots of vorticity magnitude as viewed from underneath, with the downstream lip of the cylinder ($\psi = 0$) located on the left side of each image. Perpendicular black lines through this view indicate the locations of the slices shown in Fig. 7. The slices are purposely chosen slightly off-center in order to intersect significant features of the flow. Columns (iv) and (vi) in Fig. 7 show slices of signed $\lambda_{2D,x}$ and ω_x, respectively, in the y–z plane at $x/D = 0.10$, while plots in columns (v) and (vii) show slices of signed $\lambda_{2D,z}$ and ω_z in the x–y plane at $z/D = 0.17$. The time intervals are spaced equally, except for the interval between the first (a) and second (b) rows, which is slightly shorter. Four frames are omitted between each of the last four realizations shown. Much of the following discussion is based upon close examination of movies from multiple viewpoints that contain all time frames.

At $t^* = 2.13$ (Figs. 6a, 7a), the primary ring is inclined slightly, with an angle approximately half that of the cylinder exit. In addition, the normalized ring circulation (Γ/U_0D), calculated using the line integral of velocity, of the primary ring is greater on the $\psi = \pi$ (upstream lip) side (0.86) than on the $\psi = 0$ (downstream lip) side (0.32). Both of these findings are consistent with the observations and values determined by Webster and Longmire (1998) at similar Reynolds number. These plots also reveal the presence and complex interaction of two trailing structures. Vortical structures can be seen extending from within the cylinder, down through the center of the primary ring.

After the piston stops moving, surrounding fluid is drawn inward from all sides toward the cylinder axis initiating a stopping ring (aqua) of rotation opposite to that of the primary ring. As the stopping ring forms, it is deformed by a strong sweep of fluid that moves from $\psi = \pi$ at an angle downward toward $\psi = 0$. The upstream end (near $\psi = \pi$) of the stopping ring is postulated to be induced upward into the cylinder, while the downstream end (near $\psi = 0$) becomes caught in the primary circulation and begins to be wrapped around the primary ring. This happens because the downstream end of the stopping ring is very close to the primary ring when it forms while the upstream end is not.

The green vortical structure depicted in Fig. 6a-i, which we postulate forms a ring, extends from within the cylinder down through the stopping vortex (aqua), and intersects with the downstream side of the primary ring near $\psi = 3\pi/4$ and $5\pi/4$, where it is beginning to wrap around it. The green ring results from the tubes initiated by the sweep of fluid caused by the asymmetry in the cylinder exit. The stopping vortex extends from within the cylinder downward near the $\psi = 0$ side of the primary ring, which is

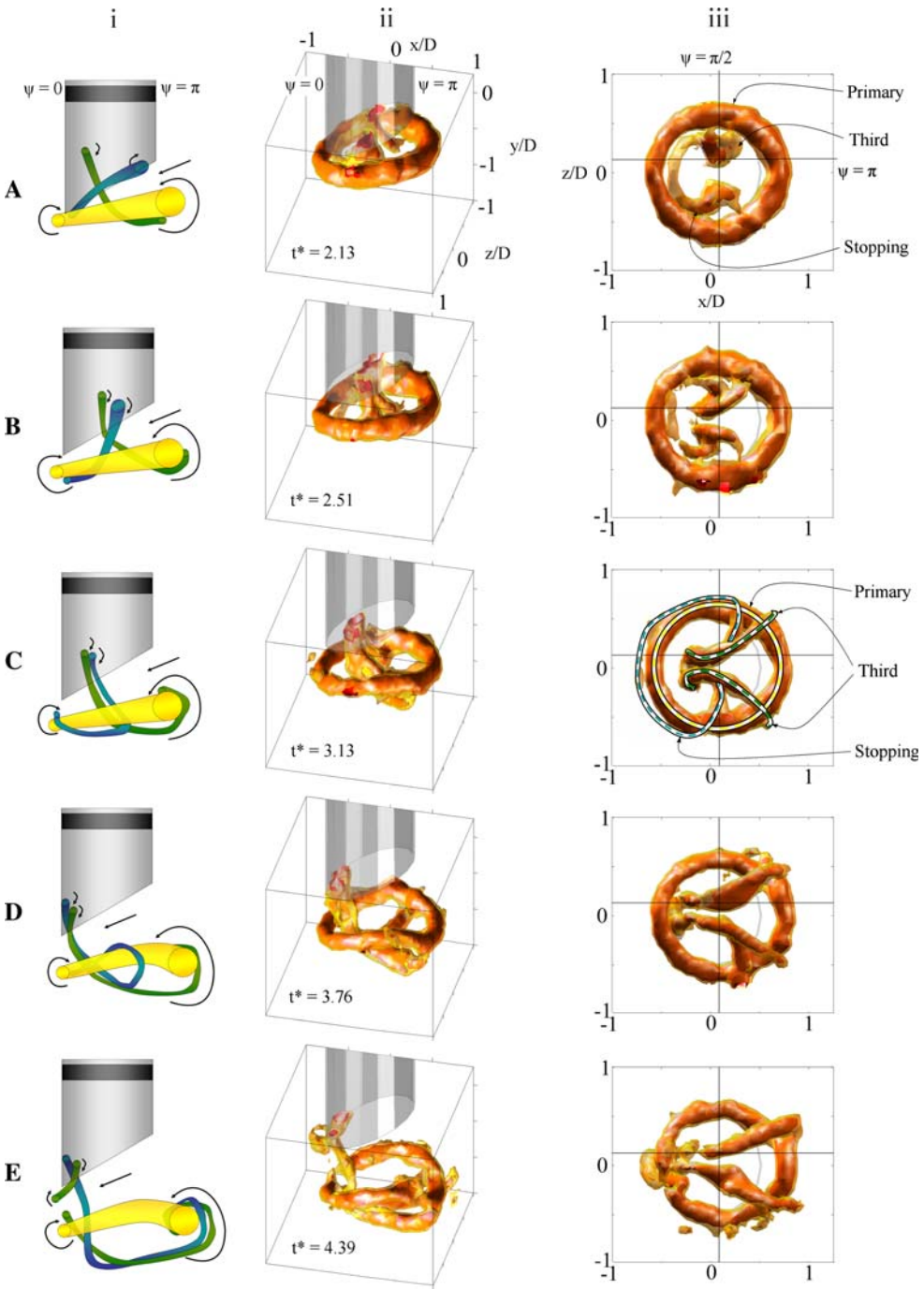

Fig. 6 Time progression (*top* to *bottom*) of vortex interactions for the $D/2$ inclined cylinder. Column (*i*) is the schematic representation. Column (*ii*) is the ω isosurfaces with the view from the side. Column (*iii*) is the ω isosurfaces with the view from underneath. Isosurface values are $\omega D/U_0 = 4.4$ (*orange*) and 6.1 (*red*). Times are $t^* =$ (**a**) 2.13, (**b**) 2.51, (**c**) 3.13, (**d**) 3.76, and (**e**) 4.39

especially evident from the bottom view in Fig. 6a-iii, where the partial stopping vortex ring is located inside of the primary ring. Figure 7a-iv contains opposite-signed (blue and red) cores of $\lambda_{2D,z}$ near the locations of $z/D = \pm 0.625$ and $y/D = -0.2$ (red) and -0.5 (blue) indicating the cross section of the primary ring. The corresponding plot of ω_z (Fig. 7a-vi) reveals additional vortical structures present in this x–y plane that are not present in the $\lambda_{2D,z}$ plot, indicating that these are swirling structures with cores at shallow angles to the plane, namely, sliced portions of the stopping ring (pink, adjacent to the right of the blue primary core) and piston ring (blue, adjacent to the left of the red primary core), which are labeled in the plot. Plots of λ_{3D} in this plane (not shown) reveal that this vorticity is indeed a result of swirling and not merely shearing motion. The y–z slice of 2D swirl plotted in Fig. 7a-v reveals portions of all three vortical structures, which are labeled in the plot. Inside of the primary ring are counter-rotating structures at nearly the same y location (parts of the green vortex ring), and above the primary ring

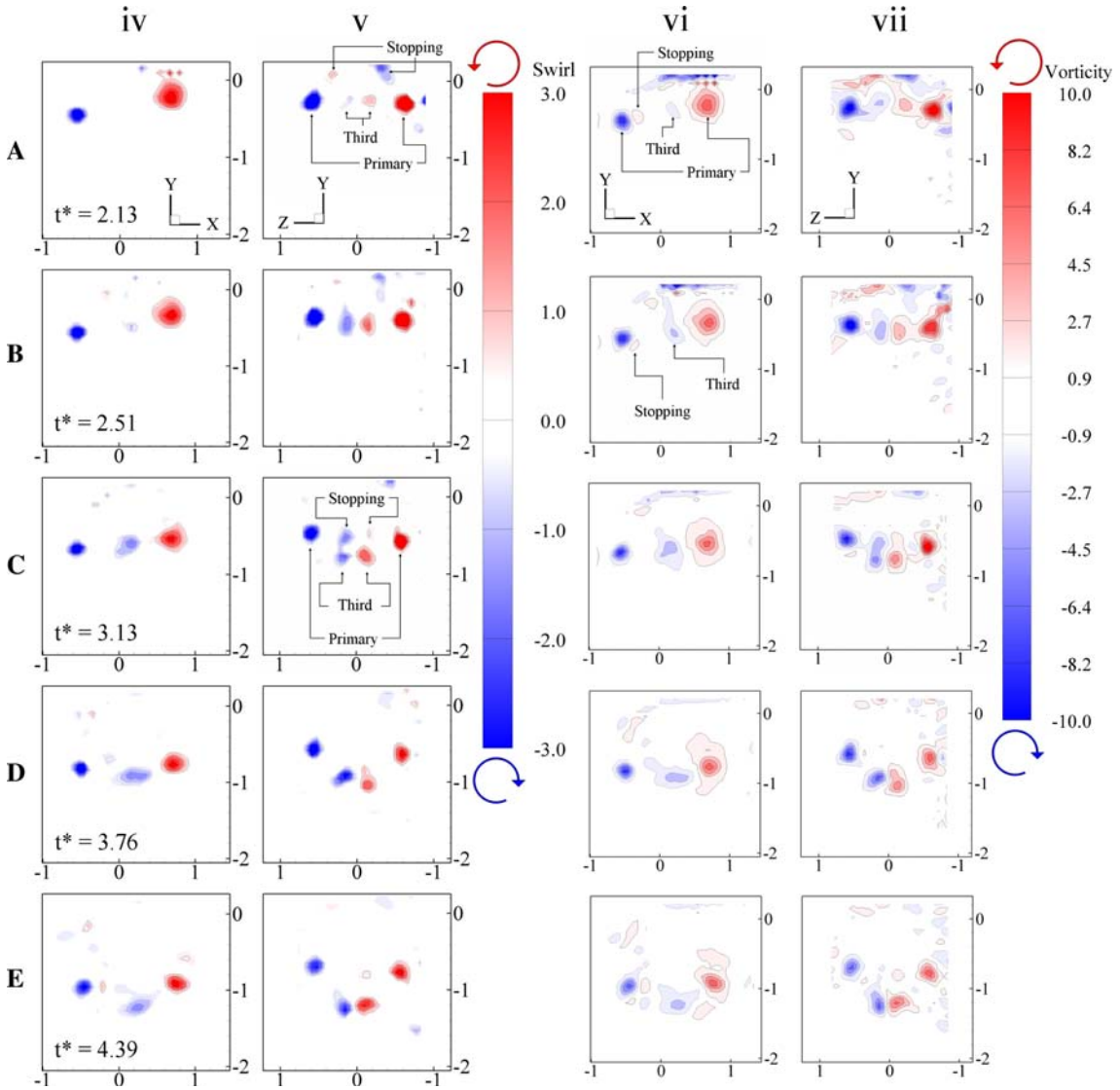

Fig. 7 Time progression (*top* to *bottom*) of vortex interactions for the $D/2$ inclined cylinder. Columns (*iv*) and (*vi*) show slices of ω_x and $\lambda_{2D,x}$ along the $x/D = 0.10$ plane, and columns (*v*) and (*vii*) show slices of ω_z and $\lambda_{2D,z}$ along the z/D 0.17 plane (plane locations are also shown as *black lines* in column (*iii*) of Fig. 6). Times are $t^* =$ (**a**) 2.13, (**b**) 2.51, (**c**) 3.13, (**d**) 3.76, and (**e**) 4.39

near $y/D = 0.1$ are counter-rotating structures associated with the stopping ring. At this t^*, the green and stopping rings have opposite sign. In Fig. 7a-vii, ω_x shows extended zones of vorticity associated with the green and stopping ring cores, indicating that additional parts of these vortices intersect the measurement plane, but at angles that are not normal to the plane.

At $t^* = 2.51$ (Figs. 6b, 7b), the two trailing structures have come together inside of the cylinder and extend into the field of view down through the center of the primary ring as seen in Fig. 6b-ii, iii. Both the third ring (green in the schematic) and the stopping ring (aqua) are beginning to wind around the primary ring. Figure 7b-vi shows a labeled portion of the stopping ring (small patch of red ω_z at $x/D = -0.4$) as it is wrapping downward around the primary ring (blue ω_z). In the y, z planes (Fig. 7b-v, vii), the cores associated with the third ring continue to be convected downward through the center of the primary ring.

At $t^* = 3.13$, in Fig. 6c-i, the leading portions of both trailing rings have now been wrapped around the primary ring (on opposite ends) and continue to wind around it. It is interesting that the wrapping of the stopping ring around the primary ring near $\psi = 0$ helps explain the circulation measurements in Webster and Longmire's Fig. 9. Their measured 'primary' circulation at $\psi = 0$ was less than that at $\psi = \pi/2$, and this would occur if the opposing circulation of the stopping core was included at $\psi = 0$. The sweeping fluid due to the asymmetry of the cylinder exit causes the upstream branches of both the third (green) and stopping rings, which extend up into the cylinder exit, to be

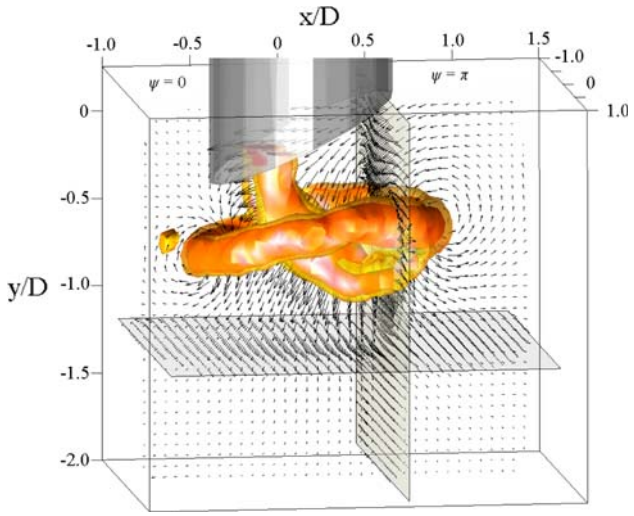

Fig. 8 Instantaneous velocity vectors for the $D/2$ cylinder at $t^* = 3.13$ (same field as Fig. 6c). Isosurface values are $\omega D/U_0 = 3.3$ (*orange*) and 6.1 (*red*)

convected toward the $\psi = 0$ side of the cylinder. In Fig. 6c-ii, though the plotted isosurface appears discontinuous, a small patch of vorticity is seen just outside of and slightly upstream of the primary ring near $\psi = 0$ at $(x/D, y/D, z/D) = (-0.7, -0.5, -0.1)$, representing part of the continuous stopping ring. (The propagation of this structure is clearer in Supplementary Movies 2a and 2b.) Sketches of the locations of the three rings are overlaid on Fig. 6c-iii. Due to the like circulation within the upstream branches of the two trailing structures, they begin to wrap around each other, with the branches of the stopping ring being drawn in through the branches of the third ring. This is evident in the progression from $t^* = 3.13$ (Fig. 6c-iii) to $t^* = 3.76$ (Fig. 6d-iii), where at the center of the primary ring, two isosurfaces of vorticity are seen winding around each other in both the top and the bottom halves of the plot ($+z/D$ and $-z/D$). Figure 7c-v has the locations of the three structures labeled. Notice that, in this cross section, the rings now all have similar sign, with clockwise swirl $\lambda_{2D,x}$ (blue) on the $-z/D$ side and counterclockwise $\lambda_{2D,x}$ (red) on the $+z/D$ side. This is in contrast to the orientation in Fig. 7a-v, where the stopping ring had sign opposite that of the other rings. This is due to the fact that from $t^* = 2.13$ to 3.13, the upstream portion of the stopping ring has become inverted from its original orientation. The sequence up to this time explains the presence of the two 'inner' pairs of cores observed in Webster and Longmire's Fig. 10 at a similar time. Further, Webster and Longmire's Fig. 10 contains a zone of opposing vorticity immediately outside of the primary core that is likely part of the stopping vortex.

At $t^* = 3.76$ (Fig. 6d), the two trailing rings continue to wrap around each other within the center of the primary ring, while simultaneously wrapping around the primary vortex ring, which becomes noticeably deformed (see Fig. 6d-ii, $\psi = 3\pi/4$ and $5\pi/4$). At $t^* = 4.39$ (Fig. 6e), the wrapping, extending, and contorting of the rings continues. In addition, the upstream portion of the combined trailing rings appears to pinch and separate. The upper portion is seen extending from the nozzle exit on the left side of both isosurface plots (Fig. 6e-ii and iii) at $\psi = 0$.

Figure 8 gives more detail of the same field and time as Fig. 6c-ii by including orthogonal slices of velocity vectors. The vectors in this plot make very clear the sweep from the upstream to downstream lip of the cylinder exit associated with the generation of additional tubes that form the third (green) vortex ring and later helps rotate the two trailing rings and causes the upstream vertically oriented vorticity branches to convect toward the $\psi = 0$ side. Webster and Longmire (1998) hypothesized a structure very similar to this figure based solely on 2D velocity slices, calling the vertically oriented sections 'branched tubes'. However, the formation mechanism of the branched tubes was difficult to observe with the available PIV data, and the presence and interaction of the stopping vortex was not considered.

Later time frames show the evolution of the intertwined structures. At $t^* = 5.02$ (Fig. 9), the two trailing rings have been extended significantly along the 0–π plane. The upstream portion of the trailing rings appears to have pinched off into a separate structure. This upstream portion of the trailing rings is seen extending from within the cylinder at the lower lip ($\psi = 0$); see also Supplementary Movies 2a and 2b. The downstream portions of both the third and the stopping rings wind and twist together to generate what looks like a single vortex ring below the primary ring. This is the structure that was postulated and

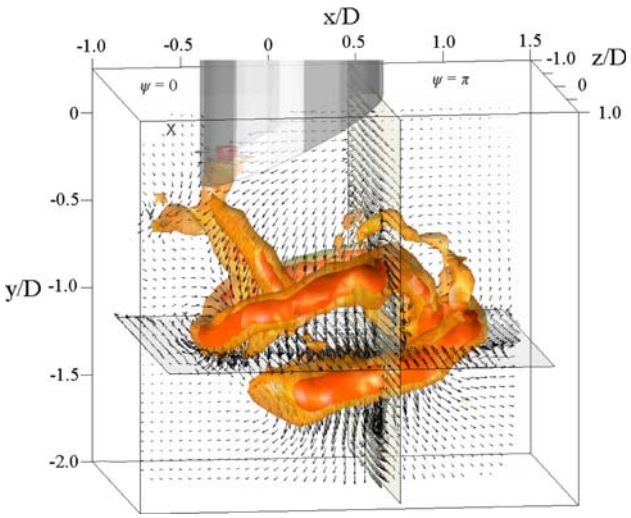

Fig. 9 Instantaneous velocity vectors for the $D/2$ cylinder at $t^* = 5.02$. Isosurface values are $\omega D/U_0 = 3.3$ (*orange*) and 6.1 (*red*)

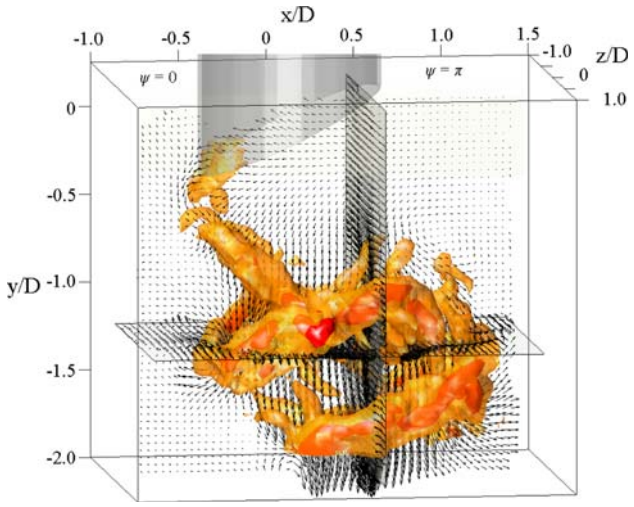

Fig. 10 Instantaneous velocity vectors for the *D*/2 cylinder at $t^* = 6.27$. Isosurface values are $\omega D/U_0 = 3.3$ (*orange*) and 6.1 (*red*)

sketched by Webster and Longmire (1998) according to their planar PIV measurements. Missing from their sketch were the upstream trailing branches of vorticity that continue to be swept downward and extend laterally in the $\psi = 0$ direction. Also, portions of the trailing rings are still loosely wrapped around the primary ring near $\psi = \pi$ as can be seen by the tubular isosurfaces of vorticity on the right side of the figure. From $t^* = 6.27$ (Fig. 10) onward, the twisted and convoluted structure continues to propagate downward, but the propagation rate is lower than for the flat cylinder case. Also, the penetration depth is reduced, and the overall motion dies out more quickly as noted by Webster and Longmire (1998). This is not surprising given the interaction between the leading and trailing circulation.

3.3 *D*/4 cylinder

Vorticity isosurfaces for flow downstream of the *D*/4 cylinder are plotted for a time sequence in Fig. 11 and depicted in Supplementary Movies 3a and 3b from $t^* = 0$ to 7.52. Note that the dimensionless times plotted are later than those shown for the *D*/2 case (Fig. 6). The flow downstream of the *D*/4 cylinder exhibited coherent vortical structures (a primary ring, a stopping ring, and a third ring) similar to those observed in the *D*/2 case, but the interactions between the primary and trailing structures were weaker, such that the two trailing rings are also drawn through the center of the primary ring, but the sweep causing this motion is weaker, and thus, the third vortex ring is weaker, and the impact of the trailing rings on the eventual shape of the primary ring is less pronounced. The trailing rings have weaker circulation, as indicated in the figure by the smaller diameter of the vorticity isosurface equal to 4.4. The movies suggest that tubes of vortical

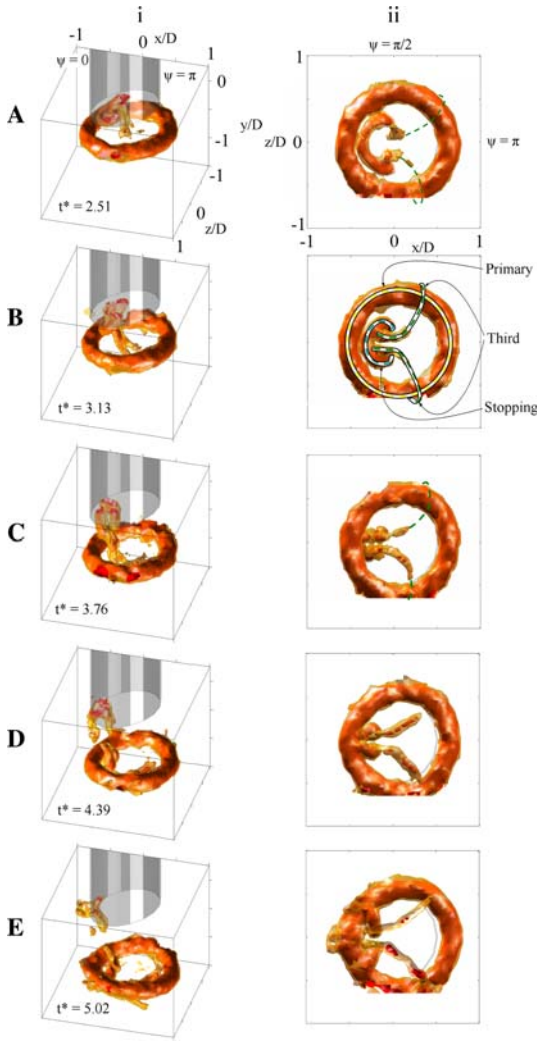

Fig. 11 Time progression of vorticity isosurfaces for the *D*/4 inclined cylinder. *Left* view from side. *Right* view from underneath. Isosurface values are $\omega D/U_0 = 4.4$ (*orange*) and 6.1 (*red*). Times are $t^* =$ (**a**) 2.51, (**b**) 3.13, (**c**) 3.76, (**d**) 4.39, and (**e**) 5.02

fluid that appear to end abruptly in Fig. 11 (e.g. Fig. 11b, c) most likely do extend to the primary ring (as indicated by the dashed lines), but the extension is difficult to see because the diameter drops below the 4 mm spatial resolution of the current dataset.

Figure 11a shows the primary ring fully formed, the downstream portion of the third ring passing through the center and winding around the primary ring, and the stopping ring just separating from the lower lip of the cylinder on the $\psi = 0$ side. Figure 11b, c, and d show the continued progression, with the stopping ring being drawn gradually downward toward the center of the primary ring through contact with vorticity associated with the third ring. Note the differences between these three plots and those in Fig. 6c, d, and e, which occur at the same t^* for *D*/2. In the *D*/2 case, the stopping ring has already begun winding around the primary

ring at $t^* = 3.13$ (Fig. 6c), while in the $D/4$ case, it does not begin this winding until about $t^* = 5.02$ (Fig. 11e). Figure 11e displays features similar to those of Fig. 7c, in which the primary ring remains mostly intact, without much deformation from its original shape, and the third ring extends from the cylinder lip through the primary ring so that it is wound around it with points of attachment near $\psi = 3\pi/4$ and $5\pi/4$. Meanwhile, the stopping ring extends from within the cylinder down through the primary ring and is just beginning the process of winding around the primary ring with points of attachment near $\psi = \pi/4$ and $7\pi/4$.

The key difference between the $D/2$ and $D/4$ cases concerns the distinctly different times at which these phenomena occur. In particular, note the longer period of time required to draw the stopping ring in through the primary ring, which is seen to begin at $t^* = 4.39$ (Fig. 11d) for $D/4$, but is already well in progress at $t^* = 3.13$ (Fig. 6c) for $D/2$. In addition, note that the upstream portion of the pinched and recombined third ring is seen emerging from the cylinder exit near $\psi = 0$ at $t^* = 5.02$ (Fig. 11e) for the $D/4$ case, as opposed to this occurring at $t^* = 4.39$ (Fig. 6e) for the $D/2$ case.

The findings at $t^* = 2.51$ (Figs. 6b, 11a) are consistent with the plots of Webster and Longmire (1998), which show the plane cutting through $\psi = 3\pi/2$ and $\pi/2$ for the $D/2$ and $D/4$ cases at $t^* = 2.62$ (their Figs. 8, 9). The planar PIV revealed two pairs of vorticity contours passing through the center of the primary ring for $D/2$, but only one pair for $D/4$. From planar PIV, the presence of the additional pair for $D/2$ and the difference in the cases were not understood clearly; however, plots from the current study make the reason for the difference quite clear, since in the $D/2$ case, both trailing rings intersect the $x/D = 0$ plane (Fig. 6b-iii), but in the $D/4$ case, only the third ring intersects the $x/D = 0$ plane at this time (Fig. 11a-ii).

4 Conclusions

Vortex rings generated from cylinders with inclined exits were studied by examining sequences of volumetric velocity fields. The current data, which show that the interaction between the trailing vortical structures and the primary vortex ring is more complicated than previously thought, give a more complete picture of the flow development, organization, and eventual breakdown mechanism. Webster and Longmire (1998) first studied these flows by examining multiple planes of standard PIV data obtained from separate flow events. From their data, they were able to reconstruct some of the most important characteristics of the flow structure. The time-evolving V3V data confirm some of their hypotheses, but also reveal significant new details on the vortex formation and interactions.

The previous data of Webster and Longmire documented the presence of trailing tubes of vorticity in addition to a dominant primary vortex ring. The V3V data show that the trailing tubes result not only from enhanced entrainment along the short cylinder side (associated with the 'third' vortex ring) but also from the stopping of the piston that drives the original impulse (associated with the stopping vortex ring). Initially, the trailing rings have rotation opposite to each other. However, the trailing rings interact with one another and the primary vortex ring such that they are distorted and rotated. Parts of the trailing rings that are eventually swept through the primary ring emerge downstream as a coherent structure resembling a secondary ring with a like sense of rotation (as depicted by Webster and Longmire). Image sequences show that additional parts extend outward, away from the primary ring in the $\psi = 0$ direction.

The V3V technique was very useful for studying this type of flow for two reasons. The first was that the acquisition of the entire instantaneous 3D velocity field allowed the placement of individual structures and events within the context and framework of the overall flow environment. The second was that the time resolution of the data allowed for tracking of the coupled evolution of dominant and secondary structures.

In particular, V3V is valuable for use in flows which exhibit highly complex 3D structures as it elucidates behavior that is difficult to resolve or understand from 2D data. The vortical interactions discussed here are much easier to track and understand by viewing movies of the events from multiple angles. In the cases presented herein, the velocity was resolved on a grid with spatial resolution of 4 mm. In order to resolve smaller scale structures (e.g. stretched trailing vortices) in the future, it would be possible to achieve finer spatial resolution by decreasing the depth of the measurement volume and increasing the number density of seed particles.

References

Allen JJ, Auvity B (2002) Interaction of a vortex ring with a piston vortex. J Fluid Mech 465:353–378

Allen JJ, Chong MS (2000) Vortex formation in front of a piston moving through a cylinder. J Fluid Mech 416:1–28

Cater JE, Soria J, Lim TT (2004) The interaction of the piston vortex with a piston-generated vortex ring. J Fluid Mech 499:327–343

Dabiri JO, Colin SP, Costello JH, Gharib M (2005) Flow patterns generated by oblate medusan jellyfish: field measurements and laboratory analyses. J Exp Biol 208:1257–1265

Didden N (1979) On the formation of vortex rings: rolling-up and the production of circulation. J Appl Math Phys 30:101–116

Gharib M, Rambod E, Shariff K (1998) A universal time scale for vortex ring formation. J Fluid Mech 360:121–140

Keane R, Adrian R (1990) Optimization of particle image velocimeters. Part 1: double pulsed systems. Meas Sci Tech 1:1202–1215

Krueger PS (2005) An over-pressure correction to the slug model for vortex ring circulation. J Fluid Mech 545:427–443

Lim TT (1998) On the breakdown of vortex rings from inclined nozzles. Phys Fluids 10(7):1666–1671

Lim TT, Nickels TB (1995) Vortex rings. In: Green SI (ed) Fluid vortices. Kluwer, Dordrecht

Ohmi K, Li HY (2000) Particle tracking velocimetry with new algorithms. Meas Sci Tech 11(6):603–616

Pereira F, Gharib M, Dabiri D, Modarress D (2000) Defocusing digital particle image velocimetry: a 3-component 3-dimensional DPIV measurement technique. Application to bubbly flows. Exp Fluids 29(suppl 1):S78–S84

Pereira F, Stuer H, Graff EC, Gharib M (2006) Two-frame 3D particle tracking. Meas Sci Tech 17:1680–1692

Shariff K, Leonard A (1992) Vortex rings. Annu Rev Fluid Mech 24:235–279

Webster DR, Longmire EK (1998) Vortex rings from cylinders with inclined exits. Phys Fluids 10(2):400–416

Zhou J, Adrian RJ, Balachandar S, Kendall TM (1999) Mechanisms for generating coherent packets of hairpin vortices in channel flow. J Fluid Mech 387:353–396